

# Insights into the Solvation and Mobility of the Hydroxyl Radical in Aqueous Solution

Edelsys Codorniu-Hernández and Peter G. Kusalik\*

Department of Chemistry, University of Calgary, 2500 University Drive NW, Calgary, T2N1N4, Alberta, Canada

**ABSTRACT:** A detailed description of the local solvation structure and mobility of hydroxyl radicals ( $\text{OH}^*$ ) in aqueous solution near ambient conditions is provided by Car–Parrinello molecular dynamics simulations. Here, we demonstrate that for HCTH/120 and BLYP functionals, smaller systems (i.e.,  $31 \cdot \text{H}_2\text{O} - \text{OH}^*$ ) are contaminated by system size effects, being biased for the presence of a three-electron two-centered hemibond structure between the oxygen atoms of a water molecule and the radical. Radial and spatial distribution functions of relatively large  $63 \cdot \text{H}_2\text{O} - \text{OH}^*$  systems reveal the existence of a 4-fold coordinated “inactive”  $\text{OH}^*$  structure with three H-bond donating neighbors and a strongly coordinated H-bond accepting neighbor. The local hydration structure around the radical exhibits more H-bond ordering than has been predicted by recent simulations employing classical force fields. Local structural fluctuations can end with spontaneous H-transfer reactions from the nearest H-bond donor water molecule, facilitated by the formation of an “active”  $\text{OH}^*$  state, resembling the proton transfer mechanism of hydrated  $\text{OH}^-$  (i.e., slight polarization of the  $(\text{H}_3\text{O}_2)^*$  complex). A comparison of the free energy barriers for the H-transfer reaction obtained by both DFT functionals and for both system sizes is also provided, demonstrating that this can be a very rapid process in water.

## 1. INTRODUCTION

The hydroxyl radical ( $\text{OH}^*$ ) has posed significant challenges to theoretical and experimental studies due to its high reactivity and very short lifetime.<sup>1</sup> However, it is still the target molecule of numerous investigations owing, in part, to its biological and atmospheric significance as well as its crucial role in industrial applications.<sup>2,3</sup> Described as the atmospheric “vacuum cleaner”, this radical is responsible for many of the reactions that remove volatile organic compounds from the air.<sup>4,5</sup> It oxidizes approximately 83% of annual methane emissions, making  $\text{OH}^*$  the most important processor of greenhouse gases.<sup>4,5</sup> Serious ailments such as cancer and Parkinson’s disease have also been related to  $\text{OH}^*$ ,<sup>6</sup> and it is recognized as the most reactive of the so-called reactive oxygen species (ROS). The only means to protect important cellular structures from its action is the use of antioxidants because, contrary to other oxidants,  $\text{OH}^*$  cannot be eliminated by an enzymatic reaction. This makes it a very dangerous compound to an organism, but interestingly,  $\text{OH}^*$  is also essential to the body’s natural defense mechanisms.<sup>6</sup>

Water apparently has a crucial role in  $\text{OH}^*$  chemistry. Recent studies have pointed out its effect on modulating  $\text{OH}^*$  reactivity, providing a clear stabilization of transition states and higher reactivity via hydrogen bonding.<sup>7,8</sup> High level *ab initio* calculations of gas phase  $\text{OH}^*(\text{H}_2\text{O})_n$  clusters<sup>9–28</sup> have also been conducted. Their focus has been on the possible existence of a  $\text{H}_2\text{O} - \text{OH}^*$  complex which is speculated to influence strongly the diffusion and oxidative capacity of the radical. Only a few studies have considered the solvation of  $\text{OH}^*$  in liquid water,<sup>29–34</sup> aimed at demonstrating an expected  $\text{OH}^*$  ability to diffuse in water via hydrogen exchange analogous to the proton-exchange reaction in the case of  $\text{OH}^-$ .<sup>30,35</sup> Prior to our work,<sup>36</sup> this key reaction had not been directly detected by either experimental or theoretical studies due to the large challenges posed by  $\text{OH}^*$  to both fields. In addition, a recent spectroscopic observation<sup>37</sup>

made during the irradiation of  $\text{OH}^-$  in aqueous solutions has been attributed to ultrafast H-transfer reactions from neighboring water molecules to  $\text{OH}^*$ . These authors<sup>37</sup> had attempted to compare their proposed mechanism with previous Car–Parrinello MD simulations<sup>31</sup> in which a three-electron two-center hemibond structure between the oxygen atom of the radical and the oxygen atom of one water molecule was found to be a particularly stable structure.<sup>30,31</sup> In the presence of the hemibond, the supposed diffusion mechanism of  $\text{OH}^*$  in liquid water via a hydrogen exchange reaction is effectively impeded.<sup>30</sup> Afterward, Vandevondele et al.<sup>33</sup> claimed that BLYP and all GGA functionals overestimate the hemibond structure and, using self-interaction corrected methods, reported that  $\text{OH}^*$  acts as a good hydrogen bond donor but accepts fewer than two hydrogen bonds on average. However, the previous apparent inability of Car–Parrinello MD to determine a  $\text{OH}^*$  H-transfer reaction<sup>29–34</sup> seems inconsistent with the low reaction barrier (around 4.2 kcal/mol)<sup>27,38</sup> predicted for the hydrogen transfer reaction in the gas phase, which is in good agreement with the available experimentally derived data.<sup>31</sup>

As we have shown in a very recent paper,<sup>36</sup> Car–Parrinello molecular dynamics simulations of a larger ( $63 \cdot \text{H}_2\text{O} - \text{OH}^*$ ) system provide a different picture with respect to previous simulations using the smaller system ( $31 \cdot \text{H}_2\text{O} - \text{OH}^*$ ).<sup>29–34</sup> Here, we present a comparison between these two systems, providing a detailed description of the solvation and electronic behavior of  $\text{OH}^*$  in aqueous solution and demonstrating that smaller systems are contaminated by system size effects. Both the HCTH/120 and BLYP density functionals are employed. Important insights into the features of the H-transfer reaction ( $\text{OH}^* + \text{H}_2\text{O} \leftrightarrow \text{H}_2\text{O} + \text{OH}^*$ ) are also provided.

Received: June 18, 2011

Published: October 03, 2011

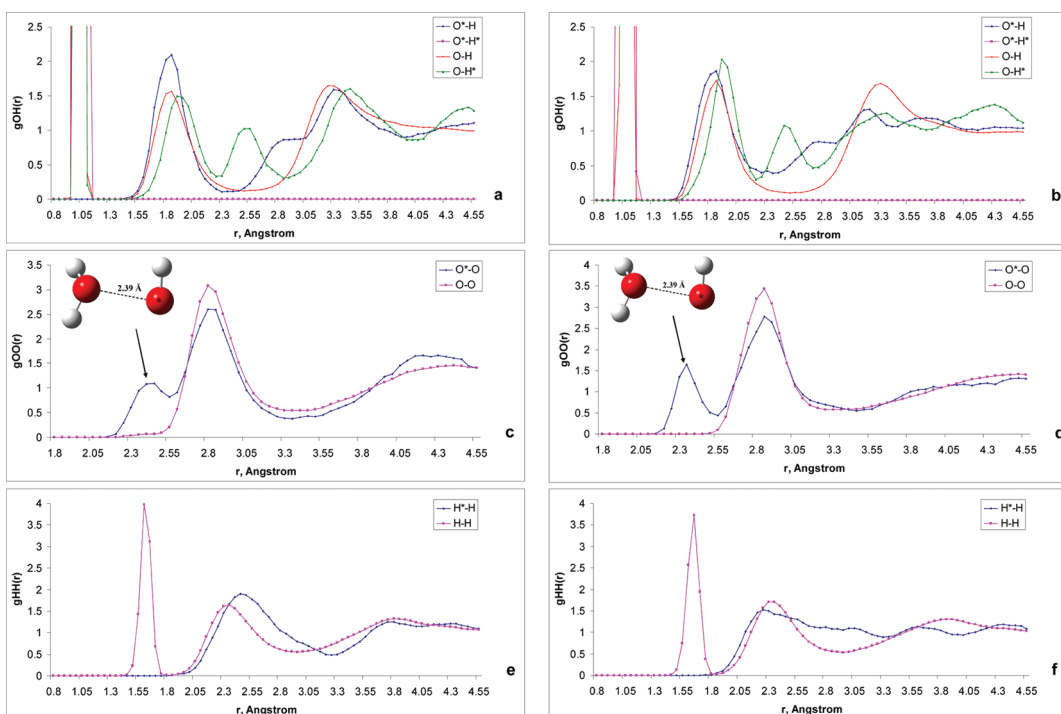


**Figure 1.** Radial distribution functions obtained with the HCTH/120 (left column) and BLYP (right column) functionals for total simulation times of 160 ps of  $31 \cdot \text{H}_2\text{O}-\text{OH}^*$  systems at a temperature of 310 K. (a, b) Oxygen–hydrogen RDFs in which  $\text{O}^*\text{H}$  is represented by a blue solid line,  $\text{O}^*\text{H}^*$  by a magenta solid line, OH by a red solid line, and  $\text{OH}^*$  by a green solid line. (c, d) Oxygen–oxygen RDFs in which  $\text{O}^*\text{O}$  is represented by a blue solid line and OO by a magenta solid line. (e, f) Hydrogen–hydrogen RDFs in which  $\text{H}^*\text{H}$  is represented by blue solid line and H–H by a magenta solid line. A representative structure for the  $\text{O}^*\text{O}$  hemibond interaction is shown in c and d.

## 2. SIMULATION DETAILS

**2.1. Car–Parrinello Molecular Dynamics Simulations.** The standard Car–Parrinello<sup>39</sup> DFT-based *ab initio* MD method was used with the CPMD<sup>40</sup> code to study  $31 \cdot \text{H}_2\text{O}-\text{OH}^*$  and  $63 \cdot \text{H}_2\text{O}-\text{OH}^*$  systems within periodic boundary conditions. The cubic simulation cells have lengths of 9.85 Å and 12.56 Å, respectively. The resulting density of 1 g/cm<sup>3</sup> corresponds to the density of water under ambient conditions. The local spin density approximation (LSDA) was employed to account for the unpaired electron at the hydroxyl radical. Two different density functionals were utilized and compared, the gradient-corrected exchange-correlation energy functionals of Becke, Lee, Yang, and Parr<sup>41,42</sup> (BLYP) and the HCTH/120.<sup>43</sup> The HCTH/120 functional was employed because it has been reported to describe accurately the properties of liquid water.<sup>43–45</sup> This particular functional is a highly parametrized GGA functional which was fit to a large set of empirical molecular properties. For our simulations, we applied the HCTH/120 functional and the Troullier–Martins norm-conserving pseudopotential,<sup>46</sup> where the valence electronic wave function is described with a plane wave basis with an energy cutoff of 90 Ry, which provides a reasonable basis set convergence for this particular system. In addition, we compare the results obtained from the HCTH/120 functional with those obtained with the BLYP functional with the Goedecker<sup>47</sup> norm-conserving pseudopotential and a valence electronic wave function described with a plane wave basis with a 75 Ry energy cutoff since this scheme was previously applied in the study of systems with 31 H<sub>2</sub>O molecules and a hydroxyl radical.<sup>29–31</sup> We use this scheme with the BLYP functional for both small ( $31 \cdot \text{H}_2\text{O}-\text{OH}^*$ ) and large ( $63 \cdot \text{H}_2\text{O}-\text{OH}^*$ ) systems for

consistency in our exploration of finite size effects. Tests with the BLYP functional in combination with either pseudopotential gave the same results. The simulations were carried out with a fictitious mass of 600 au and a simulation temperature of 310 K, whereas previous calculations employed 600 au and 800 au.<sup>31</sup> The supporting information of ref 36 explores the possible impact of the selected fictitious electronic mass for this system. We have performed a benchmarking exercise for the current methodology against non-DFT and all-electron DFT methods demonstrating that the electronic approach used in the present simulations is reasonable for our purposes. The fictitious electron kinetic energy and the dynamics of the atoms were controlled by a chain of three Nose–Hoover thermostats<sup>48</sup> operating at characteristic frequencies of 6000 cm<sup>-1</sup> and 2000 cm<sup>-1</sup>, respectively. The average fictitious kinetic energy was maintained at levels of 0.035 Ha for the  $31 \cdot \text{H}_2\text{O}-\text{OH}^*$  system and 0.06 Ha for the  $63 \cdot \text{H}_2\text{O}-\text{OH}^*$  system, both remaining stable during the whole simulation. The spin distribution function of two other systems,  $23 \cdot \text{H}_2\text{O}-\text{OH}^*$  and  $95 \cdot \text{H}_2\text{O}-\text{OH}^*$ , with dimensions of 8.4 and 14.4 Å, respectively, was calculated after geometry optimization. The input structures for the CPMD simulations were taken from a large liquid water system previously equilibrated by classical MD simulations. For these systems, a hydrogen atom was removed from the water molecule that was closest to the center of mass of the system. The first 2 ps of CPMD dynamics following the proper equilibration of the energies were also considered as equilibration and discarded. The total simulation times were 160 ps for the  $31 \cdot \text{H}_2\text{O}-\text{OH}^*$  systems and 50 ps for the  $63 \cdot \text{H}_2\text{O}-\text{OH}^*$  systems. The time step was set to 0.1 fs. Bin sizes of 0.05 Å and 5° were used for the radial and angular distribution functions, respectively. Taking into account the

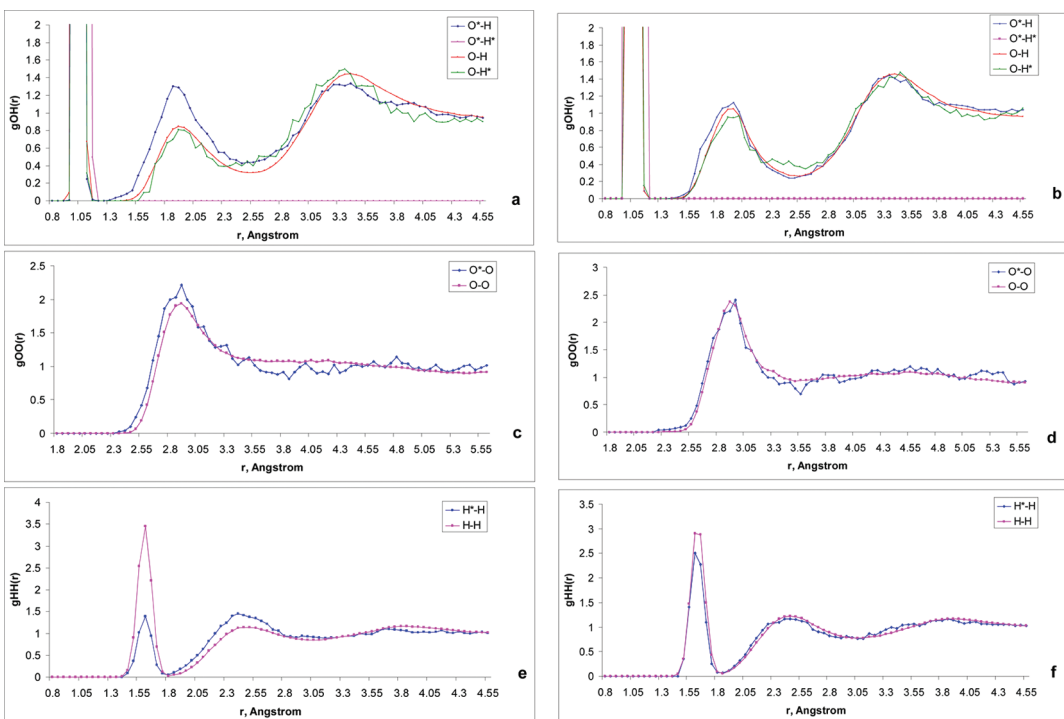


**Figure 2.** Radial distribution functions obtained with the HCTH/120 (left column) and BLYP (right column) functionals for total simulation times of 50 ps of  $63 \cdot \text{H}_2\text{O}-\text{OH}^*$  systems at a temperature of 310 K. (a, b) Oxygen–hydrogen RDFs in which  $\text{O}^*\text{H}$  is represented by a blue solid line,  $\text{O}^*\text{H}^*$  by a magenta solid line, OH by a red solid line, and OH\* by a green solid line. (c, d) Oxygen–oxygen RDFs in which  $\text{O}^*\text{O}$  is represented by a blue solid line and OO by a magenta solid line. (e, f) Hydrogen–hydrogen RDFs in which  $\text{H}^*\text{H}$  is represented by a blue solid line and HH by a magenta solid line.

importance of obtaining measures of average spatial structures<sup>49</sup> for this kind of study, a custom code was used for calculating the probability distributions of oxygen and hydrogen atoms around the  $\text{O}^*$  (or  $\text{H}^*$ ) over all system trajectories. Spherical polar coordinates were used for averaging. VMD<sup>50</sup> was utilized for visualization of configurations as well as for displaying isosurfaces. Henceforth, hydrogen and oxygen atoms from water molecules are denoted as H and O, while those from the radical are denoted as  $\text{H}^*$  and  $\text{O}^*$ , respectively.

**2.2. Constrained MD.** The free energy of the hydrogen transfer reaction between the hydroxyl radical and the water molecules was performed using constrained molecular dynamics simulations.<sup>51</sup> The difference between the  $\text{O}^*\text{H}$  and OH distances was chosen as the constraint variable R, where H is the hydrogen atom being transferred from a neighboring water molecule to the radical. For each increment ( $\sim 0.15$  Å for the  $63 \cdot \text{H}_2\text{O}-\text{OH}^*$  systems and  $\sim 0.05$  Å for the  $31 \cdot \text{H}_2\text{O}-\text{OH}^*$  systems), the average constraint force was measured over a 3 ps trajectory. From such simulations, the free energy profile may be obtained from a straightforward thermodynamic integration over the coordinate R, and the symmetry in the results was numerically imposed for the  $63 \cdot \text{H}_2\text{O}-\text{OH}^*$  system.

### 3. RESULTS AND DISCUSSION

**3.1. Solvation Structure of the  $\text{OH}^*$  in Aqueous Solution.** Significant differences can be observed in the radial, angular, and spatial distribution functions for the two studied system sizes (small,  $31 \cdot \text{H}_2\text{O}-\text{OH}^*$  and large,  $63 \cdot \text{H}_2\text{O}-\text{OH}^*$ ). The absence of a three-electron two-center hemibonded structure (between the oxygen atom of the radical and the oxygen atom

**Table 1. Coordination Numbers,  $n(r)$ , for the Hydroxyl Radical in Which the Coordination of Hydrogen and Oxygen Atoms around the Radical Oxygen Has Been Measured ( $\text{O}^*\text{H}$  and  $\text{O}^*\text{O}$ , respectively) As Well As the Coordination of Oxygen Atoms around the Radical Hydrogen ( $\text{H}^*\text{O}$ )<sup>a</sup>**

	$r$ (Å)	31 $\text{H}_2\text{O}-\text{OH}^*$		63 $\text{H}_2\text{O}-\text{OH}^*$	
		BLYP	HCTH/120	BLYP	HCTH/120
$\text{O}^*\text{H}$	1.2			0.8	1
	peak 1 ( $r$ )	2.4 (2.45)	2.1 (2.55)	3.1 (2.75)	3.2 (2.71)
	peak 2 ( $r$ )	4.4 (2.90)	4.2 (3.05)		
$\text{O}-\text{H}$	4.5	25.2	24.4	24.5	24.2
	1.2	1.9	1.9	1.9	1.9
	2.5	3.9	3.9	3.9	3.9
$\text{O}^*\text{O}$	4.5	24.9	25.2	24.8	24.9
	2.6	0.99	1.07	0.1	0.2
	3.4	4.92	4.24	4.5	4.5
$\text{O}-\text{O}$	4.5	12.2	12.9	11.3	11.5
	3.4	4.2	4.1	4.4	4.2
	4.5	12.21	12.2	11.3	11.5
$\text{H}^*\text{O}$	2.2	0.9	0.7	1.6	1.5
	2.7	1.7	1.1	2.1	2.1
	3.6	5.8	6.1	6.5	6.9
	4.5	12.9	11	12.3	12.5

<sup>a</sup> The coordination numbers of hydrogen and oxygen atoms around the water oxygen are also provided as OH and OO, respectively.

of one water molecule) in the  $63 \cdot \text{H}_2\text{O}-\text{OH}^*$  system is immediately apparent from an analysis of the radial distribution

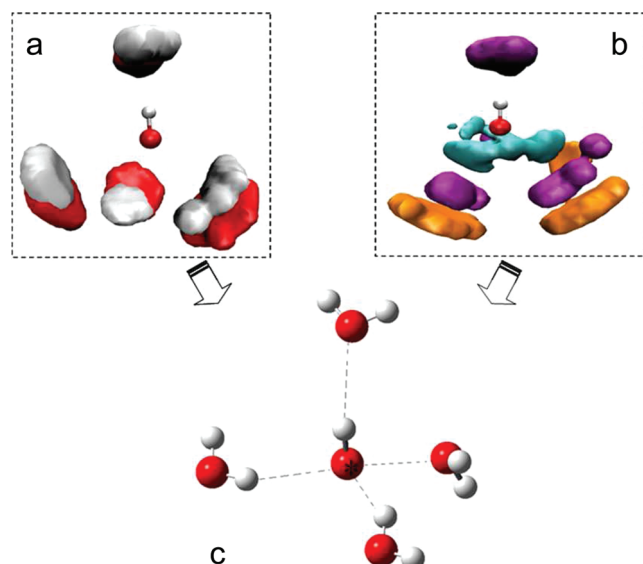


**Figure 3.** (a) Spatial distributions of hydrogen (white isosurfaces, threshold 2.1) and oxygen (red isosurfaces, threshold 3.4) atoms around the OH\* for the  $31 \cdot \text{H}_2\text{O} - \text{OH}^*$  system obtained with the HCTH/120 functional from 160 ps trajectories. We remark that the results obtained with the BLYP functional appear very similar. A 4-fold coordination of OH\* is evident in which two water neighbors donate H bonds to the radical, one water interacts through the O–O\* hemibond, and another water accepts a H bond from OH\*. (b) Spatial distributions of oxygen atoms around the OH\* for the  $31 \cdot \text{H}_2\text{O} - \text{OH}^*$  system with respect to different O\*–O separations. Color legend: cyan ( $2.3 \pm 0.25 \text{ \AA}$ ), purple ( $2.8 \pm 0.35 \text{ \AA}$ ), orange ( $4.05 \pm 0.8 \text{ \AA}$ ). The cyan isosurfaces (threshold 2.8) demonstrate that the hemibond structure is not always formed with the same water molecule, the purple isosurfaces (threshold 3.2) show the 4-fold coordination of H-bonding oxygen atoms, and the orange isosurfaces (threshold 2.4) show the spatial structure of oxygen atoms in the second solvation shell. (c) A representative snapshot configuration exhibits a typical spatial arrangement of water molecules around the radical for this smaller system.

functions (RDF) shown in Figures 1 and 2. An unusual peak in the  $g\text{O}^*\text{O}(r)$  function at around  $2.4 \text{ \AA}$  confirms the existence of this kind of interaction from both the HCTH/120 (Figure 1c) and BLYP (Figure 1d) functionals for the small  $31 \cdot \text{H}_2\text{O} - \text{OH}^*$  system; the peak does not appear with the increased size of the periodic simulation box for the  $63 \cdot \text{H}_2\text{O} - \text{OH}^*$  system (Figure 2c and d). Comparing Figures 1 and 2, we can see that the presence of the hemibond in the same system significantly alters the local structure around the radical.

The similarity of the BLYP and HCTH RDFs for both systems (Figures 1 and 2) is important to note. In the case of the  $31 \cdot \text{H}_2\text{O} - \text{OH}^*$  system, our results for the first 80 ps utilizing the BLYP functional reproduced the RDFs reported by Khalack and Lyubartsev;<sup>31</sup> however, the RDFs reported in Figure 1 averaged over a 160 ps trajectory show a more defined  $g\text{O}^*\text{O}(r)$  hemibond peak (Figure 1d) relative to the shoulder apparent in ref 31, with a consequent distortion of the  $g\text{O}^*\text{H}(r)$  in Figure 1. This confirms the persistence (i.e., stability) of the hemibond structure in  $31 \cdot \text{H}_2\text{O} - \text{OH}^*$  systems. The integration of the RDF peaks (Table 1) for this smaller system further supports the existence of a local structure very similar to those reported by Vassilev et al.<sup>30,33</sup> and Khalack and Lyubartsev,<sup>31</sup> with two H-bond donating neighbors, a H-bond accepting neighbor, and a fourth water molecule forming a hemibond. Such a structure is

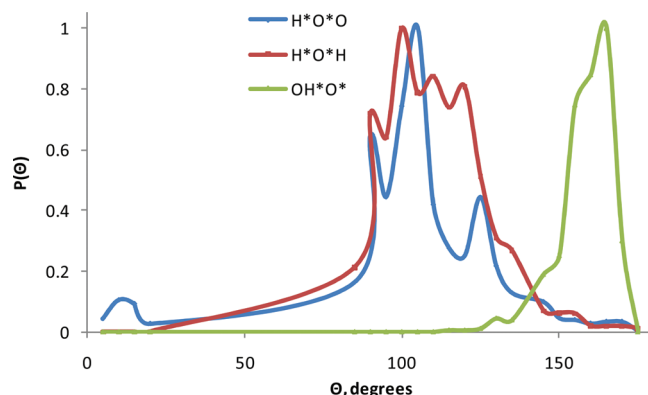


**Figure 4.** Distribution of the angles H\*O\*O (blue solid line), H\*O\*H (red solid line), and OH\*O\* (green solid line) for the first solvation shell molecules of the  $63 \cdot \text{H}_2\text{O} - \text{OH}^*$  and the HCTH/120 DFT functional averaged for 50 ps of simulation. The BLYP functional yields similar results. The blue and red lines represent the angular distribution of H-bond donating neighbors of OH\*, and the green line represents the angular distribution of the H-bond accepting neighbor of OH\*.

visualized in Figure 3, in which spatial distribution functions for the most probable locations of the nearest neighbors of the OH\* (averaged over the full 160 ps trajectories) are shown along with a representative configuration. The persistence of the hemibond appears to be rather unfavorable for the H-transfer process since no spontaneous H-transfers were observed in either of the 160 ps small system simulations.

A different local hydration structure of the radical is evident for the  $63 \cdot \text{H}_2\text{O} - \text{OH}^*$  system. It is noteworthy that in Figure 2 the OH\*–water distribution functions are generally similar to the corresponding water–water RDFs, and there is no evidence of the hemibond in the  $g\text{O}^*\text{O}(r)$  peaks (Figure 2c and d). Again, the BLYP and HCTH/120 DFT functionals yield very similar RDFs. From the integration of the RDF peaks (Table 1), it is apparent that the OH\* accepts three H bonds and donates one with water molecules in its first hydration shell. The formation of an almost tetrahedral configuration around the radical is suggested by the angular distribution functions presented in Figure 4. This structure, identified as an “inactive” OH\* state in our recent report,<sup>36</sup> can be visualized with spatial distribution functions of the most probable locations of the nearest neighbors of the OH\* (Figure 5a and b). As we shall detail below, local structural fluctuations of this “inactive”  $\text{OH}^*(\text{H}_2\text{O})_4$  can end with spontaneous H-transfer reactions in these larger systems. We note that in Figure 5a, the hydrogen atom transferred to the OH\* appears as one of the most probable locations. A representative configuration for the transfer process is shown in Figure 5c. These larger system results clearly impact our understanding of the mobility and solvation of OH\* in aqueous solution.

In addition to previous Car–Parrinello MD results, three classical MD studies have been published<sup>52–54</sup> looking to provide a description of the behavior of OH\* in aqueous solution. Classical potential models were employed and so were unable to capture the formation of the  $(\text{H}_3\text{O}_2)^*$  complex and the H-transfer reaction. Unfortunately, the potential models used apparently were not able to provide an adequate description of the specific features observed in the interaction of OH\* with water molecules. Consequently, Campo and Grigera<sup>52</sup> obtained a rather different local hydration structure for OH\* with only one H-bond water donor (53% of the time) and one H-bond water acceptor

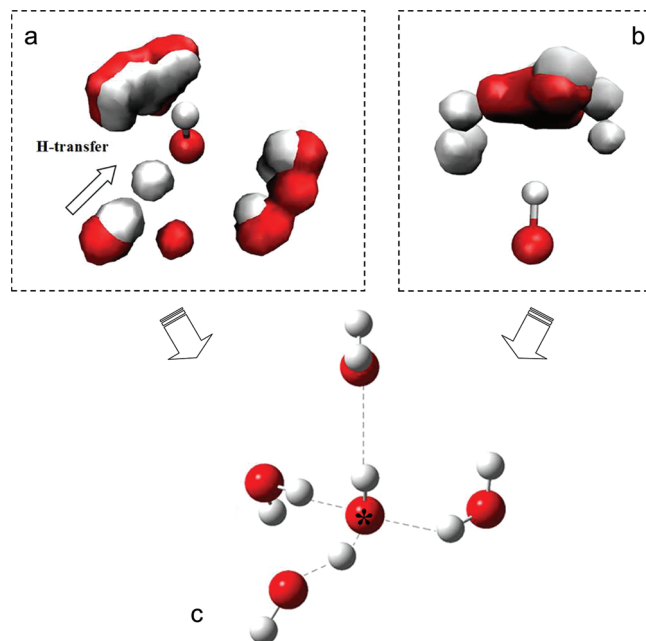


**Figure 5.** Spatial distributions of hydrogen (white isosurfaces, threshold 2.1) and oxygen (red isosurfaces, threshold 3.4) atoms around the  $\text{OH}^*$  for the  $63 \cdot \text{H}_2\text{O}-\text{OH}^*$  system obtained with the HCTH/120 functional from 50 ps trajectories. We remark that the results obtained with the BLYP functional appear very similar. (a) The isosurfaces corresponding to H-bond donating neighbors of  $\text{OH}^*$  are shown. We note that at shorter  $\text{O}^*\text{H}$  distances, the hydrogen atom position for H transfer is evident. (b) The isosurfaces for the H-bond accepting neighbor of  $\text{OH}^*$  are shown. (c) A representative snapshot configuration shows a typical spatial arrangement of water molecules around the radical during a H transfer.

(88% of the time). Svirshchev and Plugatyr<sup>53</sup> reported that  $\text{OH}^*$  occupies “holes” in the tetrahedral arrangement of water molecules, with no indication of H-bond-like arrangements. Pabis et al.<sup>54</sup> developed a flexible potential for  $\text{OH}^*$  (derived from *ab initio* gas phase  $\text{OH}^*$ –water dimer energies) and observed that the radical tends to occupy cavities in the hydrogen-bonded network of the water molecules with hydration shells of 13–14 water molecules. These striking differences from the present results again point to the importance of an adequate description of the interactions of  $\text{OH}^*$  in a water environment.

A particular RDF feature worthy of comment is the flatness of the first peak of the  $g_{\text{OO}}(r)$ , particularly for the HCTH/120 functional (Figure 2c). A previous comparison of the oxygen–oxygen RDF obtained from *ab initio* MD (CPMD) for the HCTH/120, BLYP, and BPZ functionals with experimental results has been reported by Boese et al.<sup>43</sup> These authors found the position and depth of the first minimum more shallow and shifted to a slightly smaller distance with respect to experimental data. Comparing their RDF with Figure 2c, it can be seen that the distribution function obtained here is somewhat flatter and less pronounced than that for pure liquid water. Apparently, the presence of the  $\text{OH}^*$  has perturbed the water structure somewhat.

**3.2. Size Effects and Electronic Features of  $\text{OH}^*$  in Aqueous Solution.** The marked differences observed between the RDF and SDF results for the small and large systems indicate that those from the former are contaminated by system size effects. An examination of the electronic features for both systems yields further interesting results. Different from calculations in the gas

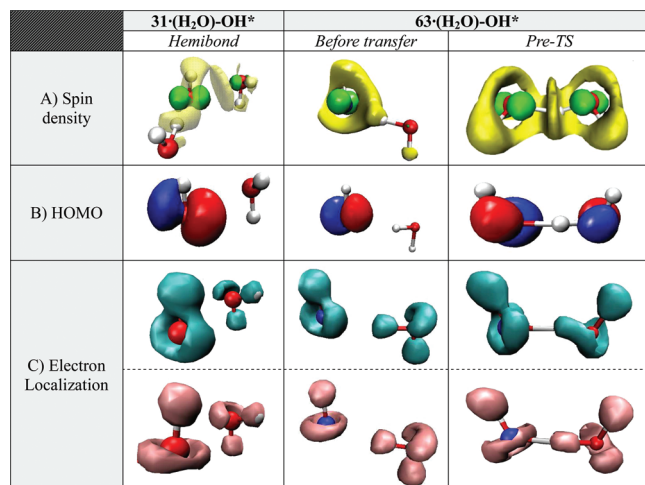


**Figure 6.** Electronic features of the three-electron two-center hemibond structure obtained with the  $31 \cdot \text{H}_2\text{O}-\text{OH}^*$  system and the spontaneous H-transfer reaction obtained with the  $63 \cdot \text{H}_2\text{O}-\text{OH}^*$  system<sup>36</sup> from the HCTH/120 functional. The BLYP functional yields similar results. Row A represents the spin density distribution with yellow (value of +0.0004) and green (value of -0.03) isosurfaces. Row B shows the evolution of the HOMO where red and blue isosurfaces have values of -0.03 and +0.04, respectively. For the smaller system, the negative HOMO isosurface points toward the hemibond oxygen. For the larger system, the HOMO is localized on the  $\text{OH}^*$  before the transfer and is perpendicular to the H bond with the nearest neighboring water molecule. In the pre-transition state, both the HOMO and HOMO-1 orbitals are shown due to the existence of  $\alpha$  and  $\beta$  degenerated states centered on the water and  $\text{OH}^*$  oxygens. Row C presents the ELF- $\alpha$  as cyan isosurfaces (threshold 0.85) and the ELF- $\beta$  as pink isosurfaces (threshold 0.85).

phase, periodic boundary conditions in MD simulations can affect certain systems, which is a possible explanation for this effect. In a  $31 \cdot \text{H}_2\text{O}-\text{OH}^*$  system, the  $\text{OH}^*$  must share its second hydration shell with its image in the periodic simulation box (being 9.84 Å in width). The highly reactive  $\text{OH}^*$  can potentially “sense” its image, allowing electronic artifacts and “undesirable” structures for the hydrated  $\text{OH}^*$  to arise during the simulation. We note that at the end of the geometry optimization step there is a spin delocalization in smaller systems ( $23 \cdot$  and  $31 \cdot \text{H}_2\text{O}-\text{OH}^*$ ), while for the  $63 \cdot$  and  $95 \cdot \text{H}_2\text{O}-\text{OH}^*$  systems, the spin density is primarily concentrated on the  $\text{OH}^*$ . Changes to the plane wave cutoff (90 Ry, 100 Ry, 120 Ry) do not alter this behavior, supporting the conjecture of a system size effect as the origins for this artifact. In our case, the selection of the  $63 \cdot \text{H}_2\text{O}-\text{OH}^*$  system implies a necessary compromise between accuracy and computational expense.

The finite size effects in MD simulations of the smaller  $31 \cdot \text{H}_2\text{O}-\text{OH}^*$  system are manifested as a persistent hemibonded structure, which is apparently a rather unfavorable structure for H abstraction. Further to the description of the electronic features during the H-transfer reaction we provided very recently,<sup>36</sup> here we focus on a comparison of the electronic properties of the  $63 \cdot \text{H}_2\text{O}-\text{OH}^*$  system with those of the  $31 \cdot \text{H}_2\text{O}-\text{OH}^*$  system (Figure 6). The spin density isosurface obtained for the smaller system evidences that the singly occupied  $p\pi$  MO of the  $\text{OH}^*$  is tied down in this hemibond; both the water and the  $\text{OH}^*$  share negative and positive spin density, consistent with a stabilizing resonance in which the electron pair is on the water oxygen atom

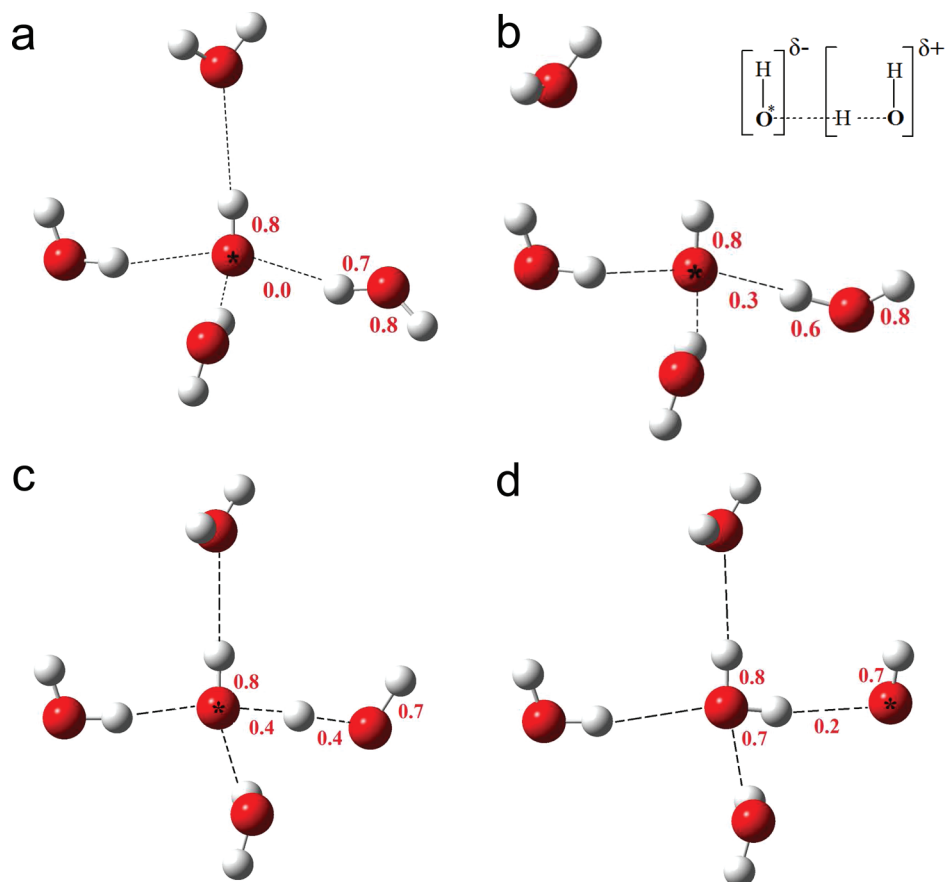


**Figure 7.** Schematic molecular configurations for different states during the spontaneous H-transfer reaction for the  $63 \cdot \text{H}_2\text{O}-\text{OH}^*$  system. (a) The initial state; (b) the pre-transition state, where the polarization of the structure is represented in the inset; (c) the transition state, a  $(\text{H}_3\text{O}_2)^*$  complex; and (d) the post-transfer state. The whole reaction (conversion from a–d) occurs in approximately 0.7 ps. The red numbers are the bond orders for the radical and the water molecule involved in the reaction.

while the unpaired electron is on the  $\text{OH}^*$  oxygen, or vice versa. In the case of the larger system, the spin density is primarily located on the  $\text{OH}^*$  prior to the H-transfer reaction. During the initial part of the reaction, a small portion of positive spin density is shared with the water molecule involved in the reaction (Figure 6). As we described in ref 36, a  $(\text{H}_3\text{O}_2)^*$  complex appears prior to the transition state (Pre-TS, Figure 6) in which positive and negative spin density is shared across both oxygen atoms.

The highest occupied molecular orbital (HOMO) provides an alternate description of the H-transfer reaction mechanism. The early movement of the electron was suggested<sup>36</sup> by the existence of essentially degenerated HOMO and HOMO-1, located on the  $\text{OH}^*$  oxygen and the water oxygen, respectively, in the pre-transition state. In the case of the smaller system, the existence of the hemibond seems not to relate with the location of the HOMO: Although the spin density shows that the unpaired electron is shared between the  $\text{OH}^*$  and the water molecule, the HOMO and HOMO-1 are both located only on the  $\text{OH}^*$  oxygen (see Figure 6). The electronic localization functions (ELF) presented in Figure 6 for the smaller system appear very similar to those of the larger system. These functions appear to remain localized on the  $\text{OH}^*$  and water molecule, further supporting the claim that resonance structures stabilize the hemibond rather than a chemical bonding. The  $\beta$  function (ELF\_BETA) for the  $31 \cdot \text{H}_2\text{O}-\text{OH}^*$  systems (Figure 6) exhibits a continuous ring around  $\text{OH}^*$  very similar to that for the  $63 \cdot \text{H}_2\text{O}-\text{OH}^*$

system before the transfer, and very similar to the picture obtained for the hydroxyl anion.<sup>35</sup> A p-like function for the unpaired electron appears in the ELF\_ALPHA for the  $\text{OH}^*$  for both small and larger systems, which becomes somewhat modified in the pre-transition state for the  $63 \cdot \text{H}_2\text{O}-\text{OH}^*$  system.

We have suggested<sup>36</sup> that the H-transfer reaction has characteristics of a hybrid mechanism apparently involving aspects of a hydrogen-atom transfer (HAT) and an electron–proton transfer (EPT). As the proton and the electron come from the same bond in this reaction, a HAT mechanism is expected. However, the evolution of the HOMO, ELF, and spin density suggests that an early electron movement occurs in the pre-transition state when the hydrogen atom (or proton) is still closer to the water oxygen. A schematic representation of the local structure of the  $\text{OH}^*$  during different states of this reaction is presented in Figure 7, along with the bond orders for the  $\text{OH}^*$  and the water molecule involved in the transfer. The three spontaneous events observed during the two simulations of the larger system all exhibited the same basic structural pattern. Figure 7a shows the “inactive”  $\text{OH}^*(\text{H}_2\text{O})_4$  state already introduced in Figure 5a. A key point in this reaction appears to be related with a change of the  $\text{OH}^*$  hydration structure from the “inactive” to the “active”  $\text{OH}^*(\text{H}_2\text{O})_3$  form (see Figure 7b). In the “active” state, the H-bond of the accepting neighbor to the  $\text{OH}^*$  becomes significantly weakened.<sup>36</sup> Interestingly, a slight polarization of the  $(\text{H}_3\text{O}_2)^*$  complex is evident at this point, while the hydrogen

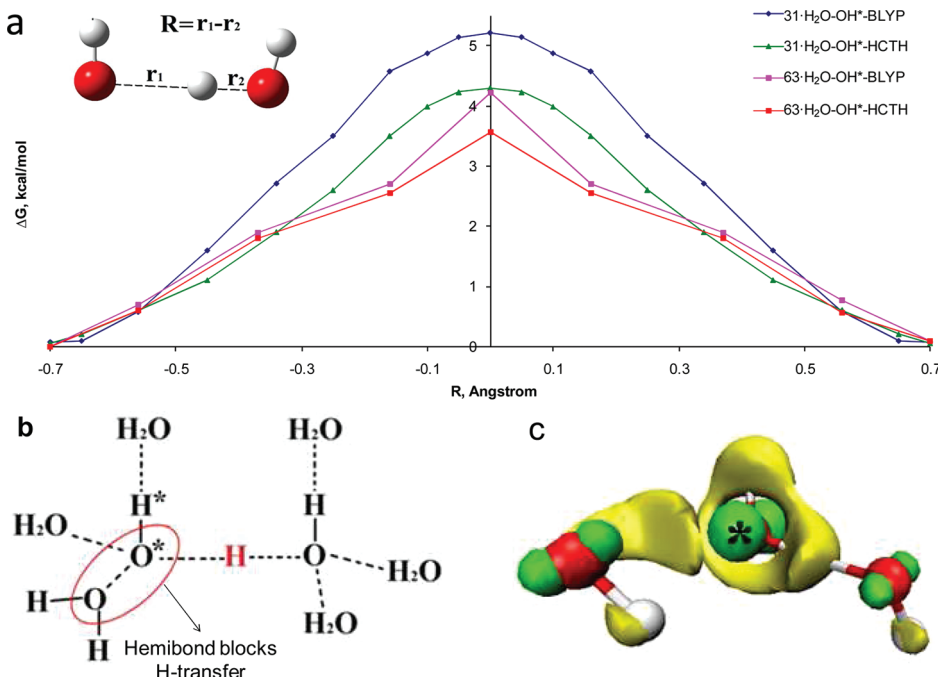


**Figure 8.** Results of constrained molecular dynamic simulation for the H-transfer reaction between OH<sup>\*</sup> and a neighboring water molecule. (a) Free energy profiles using the BLYP density functional for the 31·H<sub>2</sub>O-OH<sup>\*</sup> system (blue line) and the 63·H<sub>2</sub>O-OH<sup>\*</sup> (magenta line)<sup>36</sup> and the HCTH/120 density functional for the 31·H<sub>2</sub>O-OH<sup>\*</sup> (green line) and 63·H<sub>2</sub>O-OH<sup>\*</sup> (red line)<sup>36</sup> utilizing R as the displacement coordinate. The estimated error is in the range of 0.1–0.2 kcal/mol, obtaining by comparing forward and reverse reaction pathways as well as considering the symmetry of these functions. (b) The transition state structure obtained with BLYP (31·H<sub>2</sub>O-OH<sup>\*</sup>) shows that the hemibond structure persists even with the use of structural constraints and apparently contributes to the higher value of the energy barrier for this small system. (c) The spin density corresponding to the transition state in b is shown as yellow (value of +0.0004) and green (value of -0.03) isosurfaces and attests to its delocalization among the radical, the hemibonded water, and the water involved in the H transfer.

atom (or proton) is still not fully shared between the two oxygens (see schematic representation in Figure 7c). Consequently, the “active” states of both OH<sup>\*</sup> and OH<sup>-</sup> are similar, where the H-transfer mechanism for OH<sup>\*</sup> has key elements that resemble the proton transfer mechanism of hydrated OH<sup>-</sup>. Yet, from an analysis of constrained MD trajectories with the smaller systems for either of the functionals used (see details below), it is evident that this polarization of the (H<sub>3</sub>O<sub>2</sub>)<sup>\*</sup> complex is not present; neither is the weakening of the H bond to the accepting neighbor. Again, the presence of the hemibond is significantly altering the observed behavior during the (imposed) H transfer.

**3.3. System Size Effects in the Free Energy Barrier for H Transfer.** As already stated, the H-transfer reaction is crucial to understanding the mobility and reactivity of the OH<sup>\*</sup> in aqueous solution. Figure 8a shows the free energy profiles obtained after averaging the values of the mean forces for the forward and reverse processes in both 31·H<sub>2</sub>O-OH<sup>\*</sup> and 63·H<sub>2</sub>O-OH<sup>\*</sup> systems for both DFT functionals. A small free energy barrier is predicted in all cases, where a value of about 4 kcal/mol was obtained for the 63·H<sub>2</sub>O-OH<sup>\*</sup> systems in good agreement with experimentally derived values<sup>11</sup> and high-level *ab initio* calculations in the gas phase (4.2 kcal/mol). We note that tests using a larger step in the thermodynamic integration (i.e., ~0.15 Å for the 31·H<sub>2</sub>O-OH<sup>\*</sup> system) do not yield substantial differences in the resulting barrier height. For the small system modeled with the BLYP functional, the free energy barrier for the reaction is somewhat higher than those obtained for the larger systems. After examining the structural features of this smaller system during the imposed H transfer, it is possible to see (Figure 8b)

that the hemibond structure between the oxygen atoms of the radical and water molecules persists to the transition state. As shown in Figure 8c, the spin density is shared across the radical, the hemibonded water, and the water involved in the imposed H transfer. The hemibond predicted by HCTH/120 for the small systems seems to be less stable (c.f. the “shoulder” in the  $g_{OO}(r)$  of Figure 1c with the more defined peak in Figure 1d). With the HCTH/120 functional, the hemibond is sufficiently weak that it does not appear to survive during the imposed H transfer, thereby allowing the smaller system to exhibit a free energy barrier similar to those obtained for the larger system. Metadynamics results previously reported<sup>36</sup> confirm that the barrier for this reaction is indeed small, having an upper bound of 6 kcal/mol.

## CONCLUSIONS

Car–Parrinello molecular dynamics simulations of OH<sup>\*</sup> in liquid water, utilizing different system sizes with 31 and 63 water molecules, reveal significant insight into the hydration and mobility of OH<sup>\*</sup> in solution. Analysis of radial and spatial distribution functions demonstrates the existence of system size effects with consequent electronic implications within MD results when using smaller systems (i.e., 31·H<sub>2</sub>O-OH<sup>\*</sup>). Smaller systems (i.e., 31·H<sub>2</sub>O-OH<sup>\*</sup>) show the presence of a three-electron two-centered hemibond structure between the oxygen atoms of a water molecule and the radical. Simulations with 63·H<sub>2</sub>O-OH<sup>\*</sup> systems show two main states in the OH<sup>\*</sup> solvation, a 4-fold coordination OH<sup>\*</sup>(H<sub>2</sub>O)<sub>4</sub> as an “inactive” state in which OH<sup>\*</sup> is donating one H bond and accepting other three H bonds from

water molecules and an “active” state with three H-bond donating neighbors and a weakly coordinated H-bond accepting neighbor. Previously studied classical models seem to underestimate the interaction of water molecules with the radical. The H-transfer reaction is apparently a very rapid process in water with a relatively small free energy barrier which can contribute significantly to OH<sup>\*</sup> mobility in aqueous solution. Further spectroscopic characterization of this reaction, critical in various scientific fields, by modern ultrafast experimental techniques is clearly warranted.

## ■ AUTHOR INFORMATION

### Corresponding Author

\*Telephone: (403)-220-6244. E-mail: pkusalik@ucalgary.ca.

## ■ ACKNOWLEDGMENT

We are grateful for the financial support of the Natural Sciences and Engineering Research Council of Canada and the Canadian Foundation for Innovation. We also acknowledge computational resources made available via WestGrid ([www.westgrid.ca](http://www.westgrid.ca)) and the University of Calgary. E.C.-H. wants to acknowledge Prof. Dr. Alberto Rolo-Naranjo for his help with the SDF code and Dr. Daniel Boese for useful discussions.

## ■ REFERENCES

- (1) Sies, H. *Eur. J. Biochem.* **1993**, *215*, 213–219.
- (2) Isaksen, I. S. A.; Dalsøren, S. B. *Science* **2011**, *331*, 38–39.
- (3) Ikai, H.; Nakamura, K.; Shirato, M.; Kanno, T.; Iwasawa, A.; Sasaki, K.; Niwano, Y.; Kohno, M. *Antimicrob. Agents Chemother.* **2010**, *54*, 5086–5091.
- (4) Seinfeld, J. H.; Pandis, S. N. *Atmospheric Chemistry and Physics: From air pollution to climate change*, 1st ed.; John Wiley and Sons, Inc.: New York, 1998; pp 204–206.
- (5) Allodi, M. A.; Dunn, M. E.; Livada, J.; Kirschner, K. N.; Shields, G. C. *J. Phys. Chem. A* **2006**, *110*, 13283–13289.
- (6) Manda, G.; Nechifor, M.-T.; Neagu, T.-M. *Curr. Chem. Biol.* **2009**, *3*, 342–366.
- (7) Mitroka, S.; Zimmeck, S.; Troya, D.; Tanko, J.-M. *J. Am. Chem. Soc.* **2010**, *132*, 2907–2913.
- (8) Vöhringer-Martinez, E.; Hansmann, B.; Hernandez-Soto, H.; Francisco, J. S.; Troe, J.; Abel, B. *Science* **2007**, *315*, 497–501.
- (9) Sennikov, P. G.; Ignatov, S. K.; Schrems, O. *ChemPhysChem* **2005**, *6*, 392–412.
- (10) Chipman, D. M. *J. Phys. Chem. A* **2008**, *112*, 13372–13381.
- (11) Dubey, M. K.; Mohrschladt, R.; Donahue, N. M.; Anderson, J. G. *J. Phys. Chem. A* **1997**, *101*, 1494–1500.
- (12) Tsuji, K.; Shibuya, K. *J. Phys. Chem. A* **2009**, *113*, 9945–9951.
- (13) Soloveichik, P.; O'Donnell, B. A.; Lester, M. I.; Francisco, J. S.; McCoy, A. B. *J. Phys. Chem. A* **2010**, *114*, 1529–1538.
- (14) Cooper, P. D.; Kjaergaard, H. G.; Langford, V. S.; McKinley, A. J.; Quickenden, T. I.; Schofield, D. P. *J. Am. Chem. Soc.* **2003**, *125*, 6048–6049.
- (15) Crespo-Otero, R.; Sánchez-García, E.; Suardíaz, R.; Montero, L. A.; Sander, W. *Chem. Phys.* **2008**, *353*, 193–201.
- (16) Du, S.; Francisco, J. S.; Schenter, G. K.; Iordanov, T. D.; Garrett, B. C.; Dupuis, M.; Li, J. *J. Chem. Phys.* **2006**, *124*, 224318–15.
- (17) Galano, A.; Narciso-López, M.; Francisco-Marquez, M. *J. Phys. Chem. A* **2010**, *114*, 5796–5809.
- (18) Autrey, T.; Brown, A. K.; Camerioni, D. M.; Dupuis, M.; Foster, N. S.; Getty, A. *J. Am. Chem. Soc.* **2004**, *126*, 3680–3681.
- (19) Hamad, S.; Lago, S.; Mejías, J. A. *J. Phys. Chem. A* **2002**, *106*, 9104–9113.
- (20) Du, S.; Francisco, J. S.; Schenter, G. K.; Garret, B. C. *J. Chem. Phys.* **2008**, *128*, 084307–8.
- (21) Engdahl, A.; Karlström, G.; Nelander, B. *J. Chem. Phys.* **2003**, *118*, 7797–7802.
- (22) Kim, K. S.; Kim, H. S.; Jang, J. H.; Kim, H. S.; Mhin, B. J.; Xie, Y.; Schaefer, H. F. *J. Chem. Phys.* **1991**, *94*, 2057–2062.
- (23) Nanayakkara, A. A.; Balint-Kurti, G. G.; Williams, I. H. *J. Phys. Chem.* **1992**, *96*, 3662–3669.
- (24) Xie, Y.; Schaefer, H. F. *J. Chem. Phys.* **1993**, *98*, 8829–8834.
- (25) Wang, B.; Hou, H.; Gu, Y. *Chem. Phys. Lett.* **1999**, *303*, 96–100.
- (26) Zhou, Z.; Qu, Y.; Fu, A.; Du, B.; He, F.; Gao, H. *Int. J. Quantum Chem.* **2002**, *89*, 550–558.
- (27) Uchimaru, T.; Chandra, A. K.; Suzuki, S.; Sugie, M.; Sekiya, A. *J. Comput. Chem.* **2003**, *24*, 1538–1548.
- (28) Gonzalez, J.; Caballero, M.; Aguilar-Mogas, A.; Torrent-Sucarrat, M.; Crehuet, R.; Sole, A.; Giménez, X.; Ollivella, S.; Bofill, J. M.; Anglada, J. M. *Theor. Chem. Acc.* **2011**, *128*, 579–592.
- (29) Vassilev, P.; Louwerse, M. J.; Baerends, E. J. *Chem. Phys. Lett.* **2004**, *398*, 212–216.
- (30) Vassilev, P.; Louwerse, M. J.; Baerends, E. J. *J. Phys. Chem. B* **2005**, *109*, 23605–23610.
- (31) Khalack, J. M.; Lyubartsev, A. P. *J. Phys. Chem. A* **2005**, *109*, 378–386.
- (32) Cabral do Couto, P.; Guedes, R. C.; Martinho-Simões, J. A.; Costa Carbra, B. *J. J. Chem. Phys.* **2003**, *119*, 7344.
- (33) VandeVondele, J.; Sprak, M. *Phys. Chem. Chem. Phys.* **2005**, *7*, 1363–1367.
- (34) Chalmet, S.; Ruiz-López, M. F. *J. Chem. Phys.* **2006**, *124*, 194502–6.
- (35) Tuckerman, M. E.; Marx, D.; Parrinello, M. *Nature* **2002**, *417*, 925–929.
- (36) Codorniu-Hernández, E.; Kusalik, P. G. Mobility mechanism of hydroxyl radicals in aqueous solution via hydrogen transfer. Manuscript submitted.
- (37) Iglev, H.; Fisher, M. K.; Gliserin, A.; Laubereau, A. *J. Am. Chem. Soc.* **2011**, *133*, 790–795.
- (38) Masgrau, L.; Gonzalez-Lafont, A.; Lluch, J. M. *J. Phys. Chem. A* **1999**, *103*, 1044–1053.
- (39) Car, R.; Parrinello, M. *Phys. Rev. Lett.* **1985**, *55*, 2471–2474.
- (40) CPMD; IBM Corp.: Armonk, NY, 2006; MPI für Festkörperforschung: Stuttgart, Germany, 2001.
- (41) Becke, A. *Phys. Rev. A* **1998**, *38*, 3098–3100.
- (42) Lee, C.; Yang, W.; Parr, R. *Phys. Rev. B* **1998**, *37*, 785–789.
- (43) Boese, A. D.; Doltsinis, N. L.; Handy, N. C.; Sprak, M. *J. Chem. Phys.* **2000**, *112*, 1670–1678.
- (44) Boese, A. D.; Martin, J. M. L. *J. Chem. Phys.* **2004**, *121*, 3405–3416.
- (45) Izvekov, S.; Voth, G. A. *J. Chem. Phys.* **2005**, *123*, 134105–13.
- (46) Troullier, N.; Martins, J. L. *Phys. Rev. B* **1991**, *43*, 1993–2006.
- (47) Goedecker, S.; Teter, M.; Hutter, J. *Phys. Rev. B* **1996**, *54*, 1703–1710.
- (48) Martyna, G. J.; Klein, M. L.; Tuckerman, M. *J. Chem. Phys.* **1992**, *97*, 2635.
- (49) Kusalik, P. G.; Svirshchev, I. M. *Science* **1994**, *265*, 1219–1221.
- (50) Humphrey, W.; Dalke, A.; Schulter, K. *J. Mol. Graphics* **1996**, *14*, 33–38.
- (51) Sprak, M.; Ciccotti, G. *J. Chem. Phys.* **1998**, *109*, 7737–7745.
- (52) Campo, M. G.; Grigera, J. R. *J. Chem. Phys.* **2005**, *123*, 084507–084507–6.
- (53) Svirshchev, I. M.; Plugatyr, A. Y. *J. Phys. Chem. B* **2005**, *109*, 4123–4128.
- (54) Pabis, A.; Szala-Bilnik, J.; Swiatla-Wojcik, D. *Phys. Chem. Chem. Phys.* **2011**, *13*, 9458–9468.